PAPER

Initially generated pure mode A in the three-dimensional wake transition of a circular cylinder

To cite this article: L M Lin 2022 *Fluid Dyn. Res.* **54** 035504

IOP Publishing | The Japan Society of Fluid Mechanics Fluid Dynamics Research
Fluid Dyn. Res. **54** (2022) 035504 (29pp) https://doi.org/10.1088/1873-7005/ac796f

Initially generated pure mode A in the three-dimensional wake transition of a circular cylinder

L M Lin

Key Laboratory for Mechanics in Fluid Solid Coupling Systems, Institute of Mechanics, Chinese Academy of Sciences, Beijing 100190, People's Republic of China

E-mail: llmbirthday@163.com

Received 17 February 2022; revised 10 May 2022
Accepted for publication 16 June 2022
Published 29 June 2022

Communicated by Professor Yasuhide Fukumoto

Abstract

The initially generated pure mode A, as a transitional stage, is investigated in the three-dimensional wake transition of a circular cylinder. Direct numerical simulations are carried out over a range of Reynolds numbers from 100 to 210. According to the different dynamic behaviors of hydrodynamic parameters and similar features in the spatiotemporal evolution of vorticity in the near wake, two stages are identified. The first, investigated here, is the initial generation of pure mode A at Reynolds numbers less than 195, while the second, already reported, is the full development of pure mode A at Reynolds numbers greater than 195. The relationship between the volume-RMS (root-mean-square) vorticity and Reynolds number indicates two critical Reynolds numbers, 145 and 195 (at most). The first critical Reynolds number denotes the initial appearance of three-dimensional instability. The second critical Reynolds number indicates the transition of pure mode A from the initially generated state to the fully developed state in the near wake. After the first critical Reynolds number, the evolution of the vorticity in the near wake and on the rear surface of the cylinder clearly shows that the appearance of pure mode A is a gradual process, rather than a sudden process accompanied by a jump in vortex shedding frequency. In particular, as the Reynolds number increases, the streamwise vorticity first appears on and near the cylinder surface, then in the shear layers, and finally in the shedding primary vortices, instead of appearing instantaneously in the shedding vortices after the instability of primary vortex cores.

Keywords: wake transition, circular cylinder, vorticity, mode A

1. Introduction

The flow past a circular cylinder is a classical topic of fluid mechanics. In particular, viscous fluid surrounds a still body with large velocity gradients at the walls. Such velocity gradients cause large viscous forces acting on the body and vorticity generated at the walls. In present fluid dynamics, the main controlling parameter is a dimensionless Reynolds number *Re*, defined by the approaching stream velocity, cylinder diameter and fluid kinematic viscosity. Over a relatively small range of Reynolds numbers, many physical phenomena occur with different dynamic behaviors (Williamson 1996a). For example, oppositely signed vorticity is first concentrated just behind the body at a Reynolds number less than approximately 50. The flow is two-dimensional (2D) and steady without lift force. Then, the primary instability with the development of unsteady Kármán vortices is observed until the Reynolds number reaches $140 \sim 190$. Meanwhile, fluid forces oscillate at a certain frequency associated with primary vortex shedding. Subsequently, when the Reynolds number is beyond 190, two typical instability modes, i.e. modes A and B, are triggered in a three-dimensional (3D) wake transition. In particular, large intermittent low-frequency wake velocity fluctuations are also observed due to the presence of large-scale spot-like vortex dislocations accompanied by mode A, i.e. mode A^* (mode A + vortex dislocations). Correspondingly, the time histories of fluid forces become very complex.

Because of the above spectacular phenomena of vortices alternately shedding from a bluff body, this area is also closely related to vortex dynamics. With the aim of understanding and controlling the wake vortex dynamics, a great number of studies have been published and reported in recent decades. Experimental measurements were carried out by Meiburg and Lasheras (1988), Yokoi and Kamemoto (1992, 1993), Williamson (1996a, 1996b), Prasad and Williamson (1997), Leweke and Williamson (1998), Luo *et al* (2003), for example. Thanks to advances in computation technology, direct numerical simulations (DNSs), adopting the finite volume method or spectral element method, have become increasingly common tools in recent decades (Meiburg and Lasheras 1988, Karniadakis and Triantafyllou 1992, Wu and Ling 1993, Persillon and Braza 1998, Darekar and Sherwin 2001, Posdziech and Grundmann 2001, Jiang *et al* 2016, 2017, 2018, Agbaglah and Mavriplis 2017, 2019, Lin *et al* 2018, 2019a, Jiang and Cheng 2019, Lin and Tan 2019b, 2022). Some theoretical methods, including linear and nonlinear stability analysis, typically for Floquet stability analysis, are sometimes adopted under certain circumstances (Barkley and Henderson 1996, Henderson 1997, Ling and Chang 1999, Barkley *et al* 2000, Posdziech and Grundmann 2001, Thompson *et al* 2001, Sheard *et al* 2003, Rao *et al* 2013, Clainche *et al* 2018, Lin *et al* 2019c).

One of the central problems in most studies is to identify the critical Reynolds number Re_{cr} and correlatively the most unstable wavelength λ in the 3D wake transition of a circular cylinder. As reported in comprehensive reviews (Williamson 1996a, Posdziech and Grundmann 2001), the first discontinuity manifested by the variation in Strouhal number *St* as the Reynolds number occurs near $180 \sim 190$ depending on experimental conditions at a wavelength of approximately 3–4 diameters. This discontinuity is hysteretic. By means of stability analysis, Barkley and Henderson (1996) obtained the critical Reynolds number $Re_{cr} = 188.5 \pm 1.0$ and the most unstable wavelength $\lambda = 3.96 \pm 0.02$. Subsequently, $Re_{cr} = 190.2 \pm 0.02$ and $\lambda = 3.966 \pm 0.002$ were obtained by Posdziech and Grundmann (2001) by investigating the flow around an infinitely long circular cylinder. Recently, such Re_{cr} was also predicted to be 190.5 and 194 through linear stability analysis (Rao *et al* 2013) and DNS (Jiang *et al* 2016), respectively.

Generally, the critical Reynolds number is closely related to a physical phenomenon. For example, when $Re \geqslant Re_{cr}$, there is a 3D wake transition (Williamson 1996a), the emergence of wavy structures developed originally from 2D vortex tubes in the wake (Posdziech and Grundmann 2001) and the appearance of mode A* wake instability (Jiang *et al* 2016). To obtain the value of Re_{cr}, different methods have been adopted. In theoretical analyses, such as Floquet instability analysis (Barkley and Henderson 1996, Posdziech and Grundmann 2001, Rao *et al* 2013), the critical Reynolds number is determined by the temporal growth rate of 3D perturbations induced in the flow field. However, in experimental and numerical observations (Williamson 1996a, Jiang *et al* 2016), the appearance of a sudden drop in the Strouhal number in the *St*–*Re* relationship is usually used to predict the critical Reynolds number.

Although the disparity in the above different Re_{cr} values is already small, there still exists a puzzling unsolved problem. According to the present definitions of the critical Reynolds number stated above, it seems that these phenomena, such as 3D vortex tubes, 3D wake transition and mode A*, suddenly appear when $Re \geqslant Re_{cr}$ but completely vanish when $Re < Re_{cr}$. It is very important to solve the puzzle because this problem closely relates to the three-dimensional instability and the physical generation mechanism of streamwise vorticity in the near wake. For now, the physical explanation commonly adopted in the occurrence of pure mode A is an elliptic instability of the primary vortex cores coupled with Biot–Savart induction in the formation of streamwise vortex pairs (Williamson 1996a, Leweke and Williamson 1998, Thompson *et al* 2001, Jiang *et al* 2016, 2018). This coupling mechanism just explains the 3D waviness of primary vortices 'suddenly appearing' in the near wake and accompanied with the generated streamwise vortices. From the perspective of vorticity as the main variable to describe the intensity of a vortex, it suggests that streamwise vorticity in these streamwise vortices is also generated by this coupling mechanism. However, as indicated in previous work (Lin and Tan 2019b), pure mode A could occur at a lower Reynolds number, although spanwise vortices seem to be undisturbed. Such phenomena manifest an obvious paradox in the previous coupling mechanism that the streamwise vorticity is already generated but the primary vortex core is still stable with 2D features at a lower Reynolds number. Moreover, if these phenomena gradually fade away in the near wake as the Reynolds number decreases, then the critical Reynolds number could be lower than that previously reported, such as $Re_{cr} = 188$–194. On the other hand, a certain physical variable, such as *St*, may not properly capture such gradual variation in the disappearance of these phenomena. The physical reason is mainly attributed to the disturbance caused by these phenomena strong enough on the sudden variation in *St*, or similar physical variables or hydrodynamic parameters. Therefore, a certain kind of variable should be proposed and applied for such transitional variation at low Reynolds numbers less than the previous Re_{cr}.

Because of no sufficient research involving the possible emergence of pure mode A in the near wake at lower Reynolds numbers less than 195 (Williamson 1996a, Jiang *et al* 2016, Lin and Tan 2019b) or before *St* suddenly jumps and primary vortex cores become unstable, the primary aim of the present study is to investigate such transitional phenomenon through DNS. If such a transitional stage exists, the spatiotemporal evolution of vorticity and its sign relationships in the near wake and on cylinder surfaces and other features can be further analyzed and compared with those in pure mode A at $Re \geqslant 195$. To avoid the possible interference of vortex dislocations in identifying this transitional stage, only one spanwise wavelength of four diameters, near the most unstable wavelength, is considered.

The rest of this paper is organized as follows. The governing equations, boundary conditions and numerical methods are first presented. Then, based on features in the time histories of fluid forces, the characteristics of the spatiotemporal evolution of vorticity in the first stage, i.e. the initially generated pure mode A, the determination of the critical Reynolds number and

the physical origins of additional vorticities in the shear layers are mainly investigated and discussed in detail. Finally, major conclusions are given.

2. Numerical simulations

2.1. Governing equations and boundary conditions

As shown in figure 1(a), the fluid flow past a fixed cylinder with a circular cross-section is studied. The fluid is incompressible with constant density ρ and kinematic viscosity ν. All body forces are conservative and then can be reduced to components of pressure.

The inertial Cartesian coordinate system, (x, y, z), is established as shown in figure 1(a). Among the axes, the x-axis (streamwise direction) is aligned to the incoming free stream with uniform velocity U_∞. The z-axis (spanwise direction) is parallel to the cylinder span. The y-axis (vertical direction) is transverse to both the free stream and the cylinder axis.

The incompressible continuity and Navier–Stokes equations in dimensionless forms are written as:

$$\nabla \cdot \boldsymbol{u} = 0, \tag{1}$$

$$\frac{\partial \boldsymbol{u}}{\partial t} + (\boldsymbol{u} \cdot \nabla)\boldsymbol{u} = -\nabla p + \frac{1}{Re}\nabla^2 \boldsymbol{u}, \tag{2}$$

where ∇ is the gradient operator, $\boldsymbol{u}$ is the velocity vector with three components (u, v, w) along their own coordinates, t is the time scaled by D/U_∞, and p is the pressure scaled by ρU_∞^2. The velocities are scaled by the free-steam velocity U_∞ and the lengths by the cylinder diameter D. Thus, all variables used in the following context are scaled by ρ, U_∞ and D.

In the present study, some main variables and parameters are involved. The vorticity $\boldsymbol{\omega}$ is defined as the curl of velocity $\boldsymbol{u}$, i.e. $\boldsymbol{\omega} = \nabla \times \boldsymbol{u}$, with three components $(\omega_x, \omega_y, \omega_z)$ along the coordinates. The vorticity equation in an inertial frame is written as:

$$\frac{\partial \boldsymbol{\omega}}{\partial t} + (\boldsymbol{u} \cdot \nabla)\boldsymbol{\omega} = (\boldsymbol{\omega} \cdot \nabla)\boldsymbol{u} + \frac{1}{Re}\nabla^2 \boldsymbol{\omega}. \tag{3}$$

As an important indicator in the present flow dynamics, variations in the drag and lift forces acting on the body are taken into account and normalized as the drag and lift coefficients, C_D and C_L, respectively. Then, the mean drag coefficient, $\overline{C}_\mathrm{D}$, and the root-mean-square (RMS) lift coefficient, C'_L, are used to determine the intensity of fluid forces. When spanwise vortices are alternately shed in the near wake, the frequency of such vortex shedding, f, is obtained through Fourier analysis of the time history of C_L and scaled as the Strouhal number, St, defined by $St = fD/U_\infty$.

For the initial condition, the flow is assumed to be motionless with $\boldsymbol{u} = 0$ and $p = 0$ at $t = 0$, except at the inlet.

For the boundary conditions, the 3D flow is first assumed to be spatially periodic across the span. At the inlet, the uniform free stream is prescribed as $u = U_\infty$ and $v = w = 0$. At the outlet, a simple outflow with $\partial \boldsymbol{u}/\partial x = 0$ is applied. At both lateral boundaries in the y-axis, free slip with $\frac{\partial u}{\partial y} = v = \frac{\partial w}{\partial y} = 0$ is adopted. On cylinder surfaces, the no-slip boundary condition with $\boldsymbol{u} = 0$ is used. The reference pressure of $p_\infty = 0$ is specified at the center of the inlet.

2.2. Computational domain and mesh

As shown in figure 1(a), the whole nondimensional computational domain for the present wake flow is described by the inlet length $L_\mathrm{I} = 20$, the outlet length $L_\mathrm{O} = 30$, the vertical height

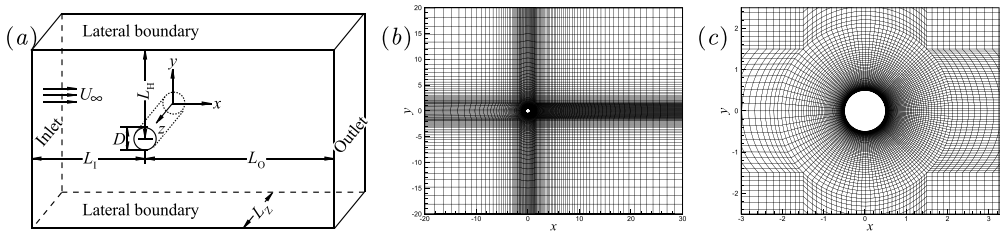

Figure 1. (a) Schematics of a flow past a straight cylinder with a circular cross-section, and computational domain in the (x, y) plane and mesh distributions in (b) the whole flow region and (c) near the cylinder with a closer view.

$L_H = 20$ and the computational spanwise length or cylinder span $L_Z = 4$. The blockage ratio β, defined by $1/(2L_H)$, is therefore 2.5%.

The mesh distribution in the 2D computational domain is presented in figure 1(b). The smallest grid size δ of 0.001 is the normal distance of the first layer of the mesh next to the cylinder surface. A local mesh is mainly refined in the large circular region with a radial diameter of approximately 4.24, as shown in figure 1(c). A coarse mesh is mainly distributed far from the cylinder. The total element number of the present 2D standard mesh, N_{xy}, is 20 100. As already analyzed and reported in previous works (Henderson 1997, Lin and Tan 2019b), a uniform spanwise grid size, $\Delta z = 0.1$, is adopted.

2.3. Numerical method

Numerical calculations are performed using FLUENT V6.3.26 software with the finite-volume method. The pressure-implicit splitting of operators (PISO) algorithm as a pressure-velocity coupling scheme is applied. For the discretization scheme, the second order is applied for the pressure equation; the second-order upwind scheme is used in solving the momentum equation; and the second-order implicit scheme is adopted in all unsteady formulations. In particular, gradient computation is solved by the Green–Gauss node-based method. Other computational settings, such as under-relaxation factors and multi-grid method, are all default.

The nondimensional error of the mass conservative equation, equation (1), reaches the order of magnitude of $O(10^{-7})$, while the dimensionless errors of the three components of the momentum equations, equation (2), are lower, on the order of $O(10^{-9})$.

The dimensionless time step Δt is 0.01. Here, the maximal cell Courant number, $Co = \Delta t|u|/\Delta l$, is less than approximately 0.8, where Δl is the cell size in the direction of the local velocity u through a cell.

2.4. Independence study

As for the independence study, some aspects are taken into account and presented as follows, also reported in previous works (Lin and Tan 2019b, 2022).

In the first aspect, the independence of 2D computational domain in the (x, y) plane, $(L_I + L_O) \times (L_H + L_H)$, is carried out at $Re = 250$ with almost same mesh resolutions, as shown in table 1 (SM, LSM and SSM). Among them, the computational domain in the 2D standard mesh, denoted by 'SM', is $(20 + 30) \times (20 + 20) = 50 \times 40$. While the large domain, denoted by 'LSM', is $(30 + 40) \times (30 + 30) = 70 \times 60$, and the small domain, denoted by 'SSM', is $(10 + 20) \times (10 + 10) = 30 \times 20$. The relative error of hydrodynamic parameters between SM

Table 1. Comparisons of hydrodynamic parameters, $\overline{C}_{\mathrm{D}}$, C'_{L} and St, among different computational domains (SM, LSM and SSM), mesh resolutions (SM, MS and MW) and the smallest grid sizes (SM, SMG2 and SMG5) in present 2D numerical simulations at $Re = 250$. Note that the numbers in parentheses represent the relative errors from the case SM.

Cases	L_{I}	L_{O}	L_{H}	N_{xy}	δ	$\overline{C}_{\mathrm{D}}$ (%)	C'_{L} (%)	St (%)
SM	20	30	20	20 100	0.001	1.3486(0.0)	0.5586(0.0)	0.2029(0.0)
LSM	30	40	30	22 850	0.001	1.3402(0.6)	0.5541(0.8)	0.2023(0.3)
SSM	10	20	10	16 400	0.001	1.3826(2.5)	0.5752(3.0)	0.2065(1.8)
MS	20	30	20	35 400	0.001	1.3451(0.3)	0.5551(0.6)	0.2021(0.4)
MW	20	30	20	25 600	0.001	1.3572(0.6)	0.5560(0.5)	0.2046(0.8)
SMG2	20	30	20	20 100	0.002	1.3500(0.1)	0.5687(1.8)	0.2023(0.3)
SMG5	20	30	20	20 100	0.005	1.3520(0.3)	0.5720(2.4)	0.2015(0.7)

and LSM is less than 1%, while that for SM and SSM is about $2\% \sim 4\%$. It demonstrates that the present computational domain, SM, is suitable for DNS.

As the second aspect, the mesh dependence is also studied at $Re = 250$ with different 2D mesh resolutions, as shown in table 1 (SM, MS and MW). Among them, the cell number around the cylinder surface is doubled as 260, and the total number of grids in such modified mesh on surface, denoted by 'MS', is 35 400. Moreover, the grid number in the wake, $x \in (2.12, 30]$, is also doubled as 100 with the cell expansion ratio reduced to 1.015. Consequently, the total number of cells in this refined mesh in the wake, denoted by 'MW', is 25 600. It is found out that the relative error is less than 1% among three different meshes of SM, MS and MW, which indicates the present mesh SM with enough mesh resolution.

On the other hand, instant profiles of streamwise and vertical components of velocity along the y-axis at different streamwise positions are compared among three meshes (SM, MS and MW), as shown in figures 2 and 3, at two typical moments, $t = T_0$ and T_1, as shown in figure 4. The present results have shown that different meshes have little effect on instant velocity profiles, particularly near the cylinder, which indicates that the physical investigation of vorticity generation and sign relationships is independent of the mesh.

As for the third aspect, the independence of the smallest grid size on the cylinder surface, δ, is investigated at $Re = 250$, as shown in table 1 (SM, SMG2 and SMG5). Among them, the smallest grid size is 0.002 in the mesh, denoted by 'SMG2', and increased up to 0.005 in the mesh, denoted by 'SMG5', without change of total grid numbers N_{xy} and computational domain $(L_\mathrm{I} + L_\mathrm{O}) \times (L_\mathrm{H} + L_\mathrm{H})$. As the smallest grid size increases, the fluid forces are gradually increased, while the vortex-shedding frequency is reduced. Except $\overline{C}_\mathrm{D}$ and St, only C'_L is varied greatly and the relative error exceeds 1%. This indicates the present $\delta = 0.001$ is suitable for present DNS because the smallest grid size is very important in capturing main characteristics of vorticity and its sign evolving near the cylinder surface.

Furthermore, in the last aspect, the St–Re relationship including 2D and following 3D computations is presented and compared with previous results, as shown in figure 5. The present 2D simulations agree well with the experimental results (Williamson 1996a). In the 3D simulations, results with $L_\mathrm{Z} = 4$ are consistent with previous simulations (Posdziech and Grundmann 2001) because of the approximate computational length L_Z. Moreover, numerical computations with $L_\mathrm{Z} = 12$ are also carried out at $Re = 190$ and 195 in order to confirm the reliability of present calculation results at $L_\mathrm{Z} = 4$. In figure 5, St at $Re = 195$ and $L_\mathrm{Z} = 12$ also agrees well with that in numerical results (Jiang *et al* 2016). While at $Re = 190$, St with $L_\mathrm{Z} = 12$ is precisely consistent with that with $L_\mathrm{Z} = 4$, which indicates that vortex dislocations have not been excited and the spanwise computational length of $L_\mathrm{Z} = 12$ has no effect on St, as well as $\overline{C}_\mathrm{D}$ and C'_L as reported in following contexts. A simple comparison about the qualitative sign of vorticity can refer to the following content.

In addition, as for 3D computations, the mesh independence of spanwise grid size $\Delta z = 0.05$ was also validated at $Re = 200$ and 300 and already reported in previous works (Lin and Tan 2019b, 2022). And the comparison of fluid forces in present 2D and 3D computations with previous works can also refer to the following content.

3. Results and discussion

3.1. Features of fluid forces

First, the time histories of fluid forces are investigated in a range of Reynolds numbers from 150 to 210. Typically, as shown in figures 6 at $L_\mathrm{Z} = 4$ and 7 at $L_\mathrm{Z} = 12$, there are two features. When $Re < 195$, the oscillating amplitudes of fluid forces are almost constant over time, which

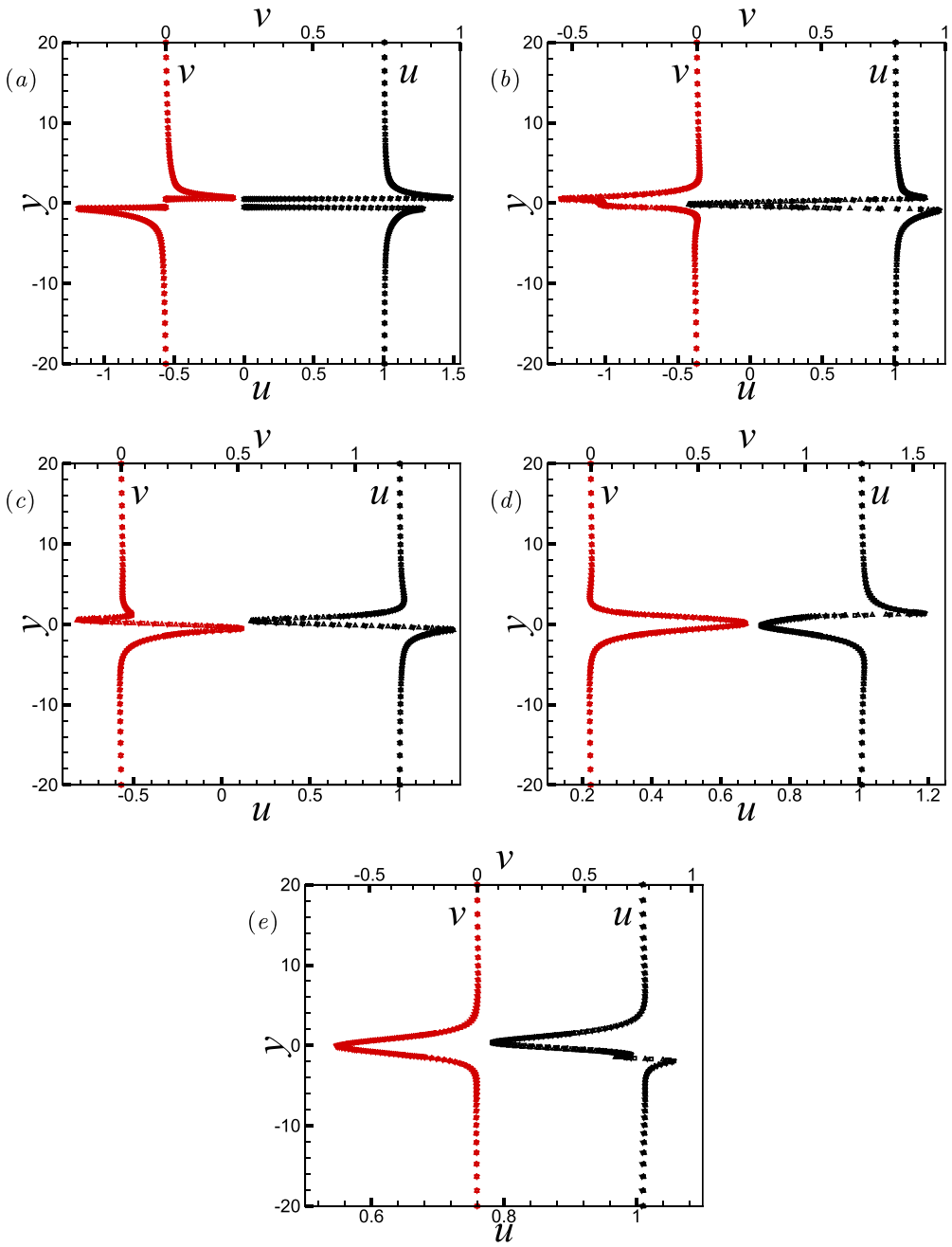

Figure 2. At $t = T_0$ (as shown in figure 4) and $Re = 250$, for comparisons among different 2D meshes, SM ('□'), MS ('△') and MW ('▽'), profiles of two velocity components (u and v) varied along the vertical direction at (a) $x = 0$, (b) 1, (c) 2, (d) 3 and (e) 5. Note that it is difficult to distinguish the difference among three meshes in all figures since the difference is so small.

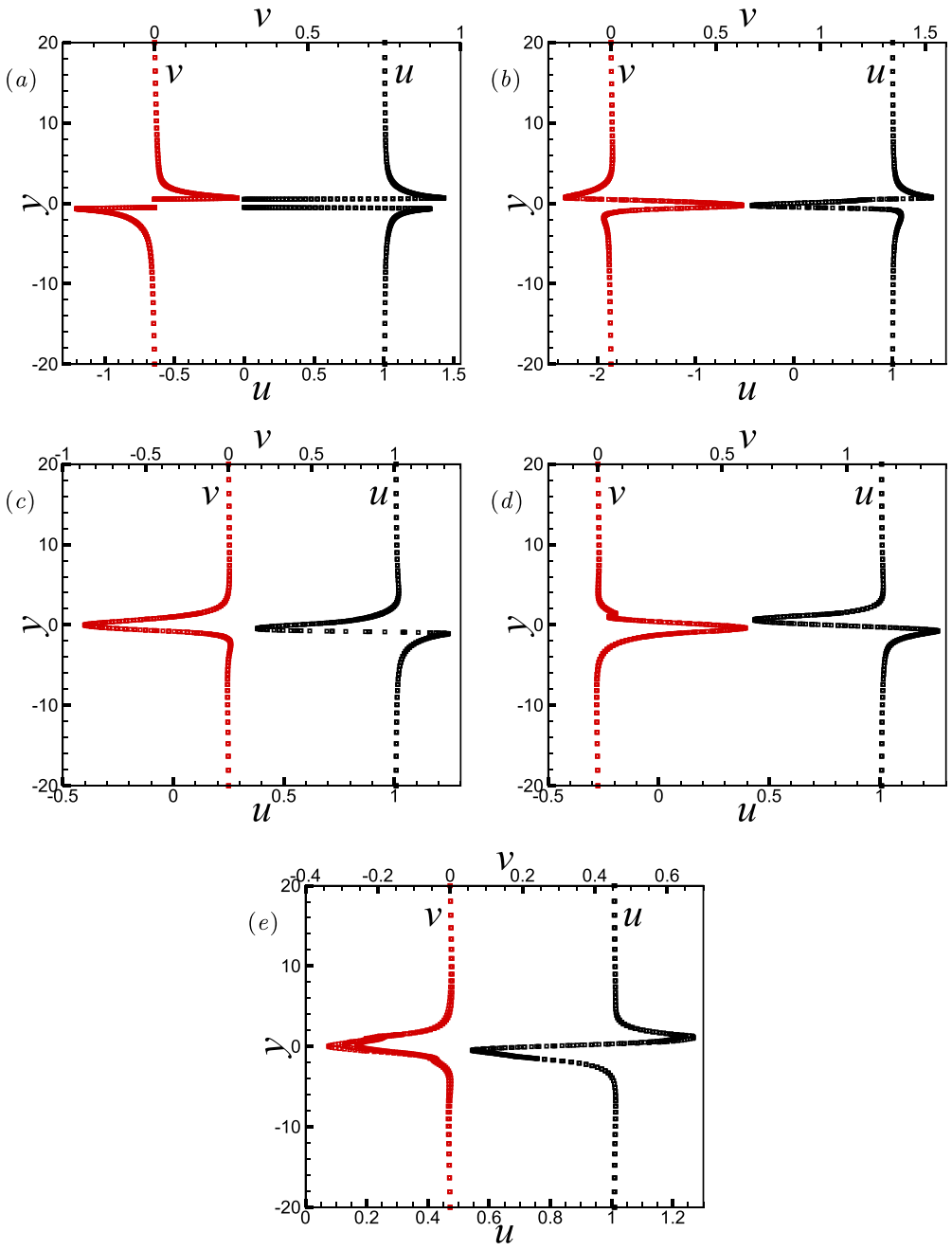

Figure 3. At $t = T_1$ (as shown in figure 4) and $Re = 250$, for comparisons among different 2D meshes, SM ('□'), MS ('△') and MW ('▽'), profiles of two velocity components (u and v) varied along the vertical direction at (a) $x = 0$, (b) 1, (c) 2, (d) 3 and (e) 5. Note that it is difficult to distinguish the difference among three meshes in all figures since the difference is so small.

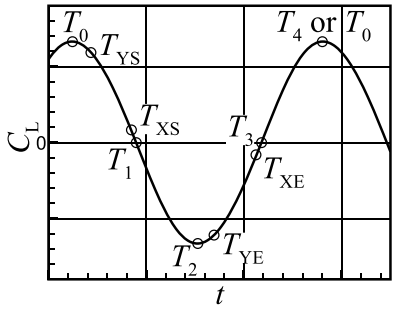

Figure 4. In the initially generated pure mode A of a circular cylinder's wake transition, schematic of a whole period or cycle of the oscillating lift coefficient with typical times, where T_0 (or T_4) and T_2 denote the positive and negative extremum values of the lift force, respectively, and both T_1 and T_3 are associated with $C_L = 0$, and T_{XS}, T_{XE}, T_{YS} and T_{YE} are related to the initial generation of streamwise and vertical vorticities in the shear layers.

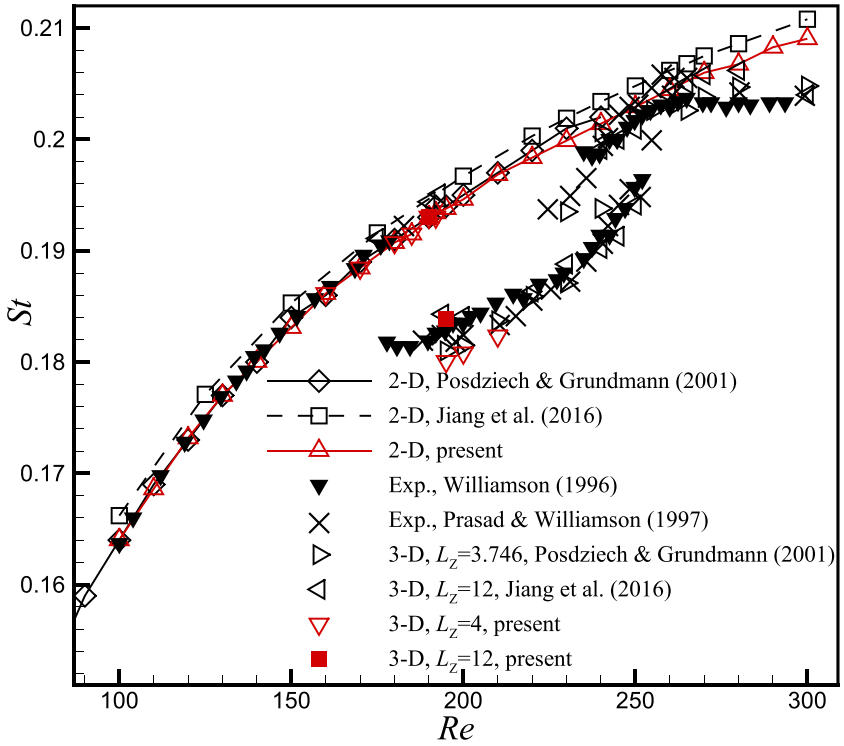

Figure 5. The *St*–*Re* relationship over 2D and 3D wake transition regimes.

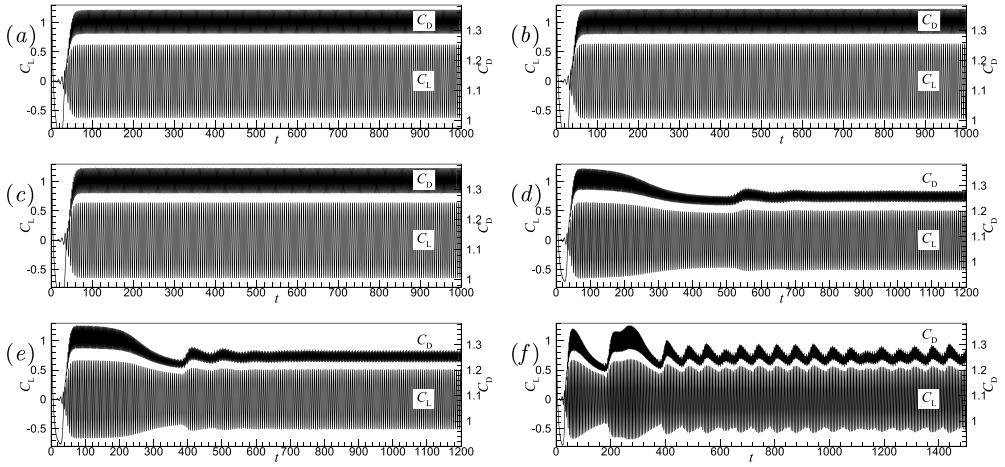

Figure 6. Time histories of fluid forces, C_D and C_L, at Reynolds numbers of (a) 185, (b) 190, (c) 192, (d) 195, (e) 200 and (f) 210 with $L_Z = 4$.

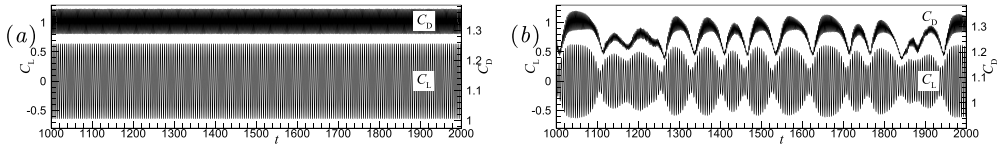

Figure 7. Time histories of fluid forces, C_D and C_L, at Reynolds numbers of (a) 190 and (b) 195 with $L_Z = 12$.

indicates that the wake flow is almost the same as the 2D flow state. At $Re \geqslant 195$, oscillating peak-to-peak amplitudes with $L_Z = 4$ are initially at a high level and then at a low level. As for fluid forces with $L_Z = 12$, the irregular appearance of vortex dislocations leads to peak-to-peak amplitudes oscillated violently. These features clearly indicate that the wake flow becomes three-dimensional. In particular, at $Re = 210$ and $L_Z = 4$, although the wake is fully developed when $t > 400$, the oscillating peak-to-peak amplitudes still vary over time.

Then, hydrodynamic parameters, i.e. the mean drag coefficient, RMS lift coefficient and Strouhal number, in the present 2D and 3D computations are presented and compared with previous results, as shown in figures 5 and 8. At $Re < 195$, these parameters are all equivalent to those in the 2D simulations. When $Re \geqslant 195$, they all drop suddenly, corresponding to the existence of pure mode A ($L_Z = 4$) or mode A* ($L_Z = 12$) in the near wake. In addition, the present mean drag coefficient and RMS lift coefficient in the 2D and 3D calculations are all in good agreement with the previous results as shown in figure 8, regardless of whether L_Z is 4 or 12.

According to the following contexts about the spatiotemporal evolution of vorticity in the near wake, to distinguish these different dynamic behaviors, two wake stages are identified. The first stage with almost 2D wake flow and invariant fluid forces at $Re < 195$ is called the initially generated pure mode A. However, when the Reynolds number is greater than 195, obvious 3D wake flow and a sudden drop in fluid forces with $L_Z = 4$ are referred to as the fully developed pure mode A, as the second stage. The detailed investigation into the fully developed stage of pure mode A can be referenced in a previous work (Lin and Tan 2019b).

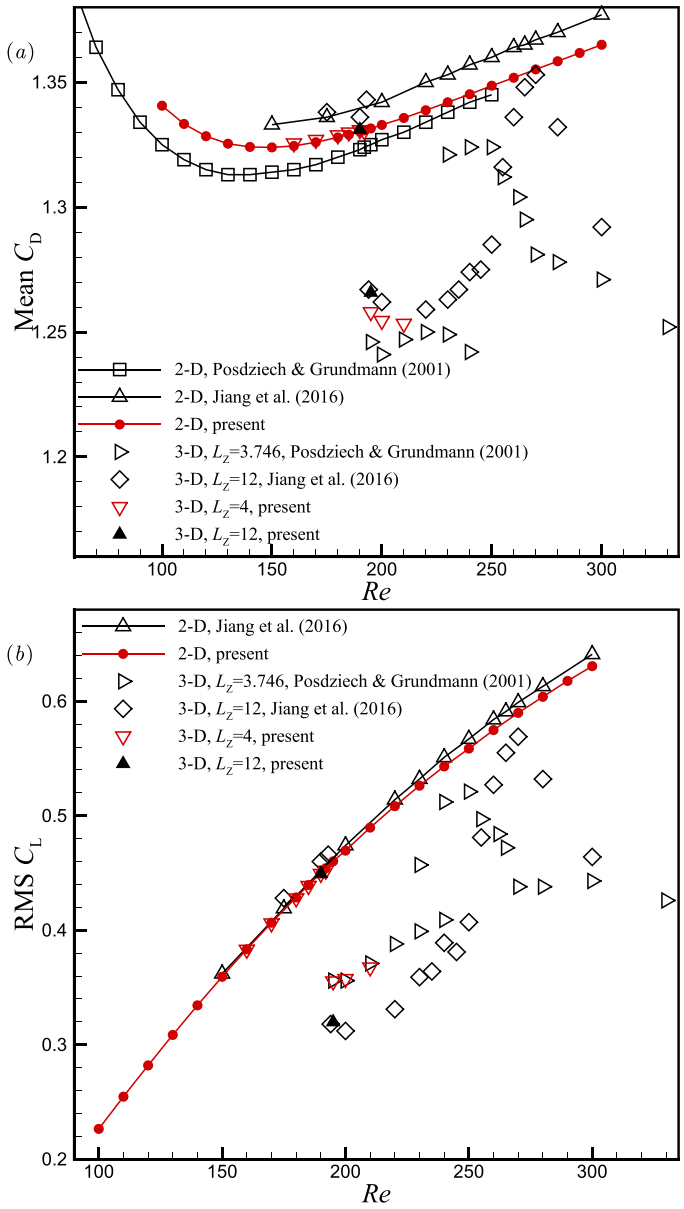

Figure 8. (a) Mean C_D and (b) RMS C_L varied along the Reynolds number in the present 2D and 3D computations.

Here, the main focus is put on the initially generated stage in a range of Reynolds numbers from 150 to 195 with $L_Z = 4$.

3.2. Evolution of the vorticity and its sign relationship

First, it should be noted that only additional vorticities, ω_x and ω_y, with magnitudes of at least 0.001 are presented in order to avoid possible contamination or interference caused by

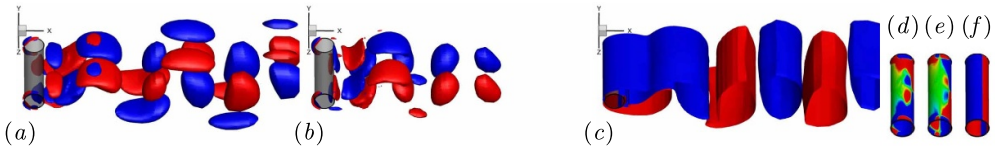

Figure 9. At $t = T_0$, isosurfaces of (a) $\omega_x = \pm 0.02$, (b) $\omega_y = \pm 0.02$ and (c) $\omega_z = \pm 0.2$, and contours of (d) ω_x, (e) ω_y and (f) ω_z on cylinder surfaces at $Re = 190$ with $L_Z = 4$, where red and blue colors denote positive and negative values, respectively, and green color denotes $|\omega| < 0.001$. Note that the cylinder is denoted by the grey translucent surface in iso-surfaces.

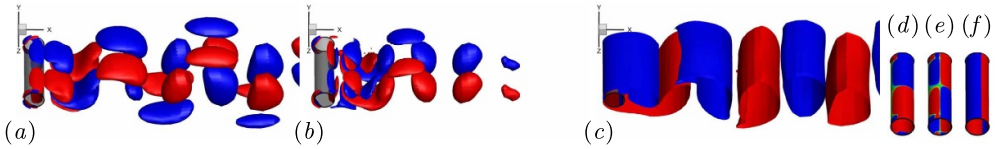

Figure 10. At $t = T_1$, isosurfaces of (a) $\omega_x = \pm 0.02$, (b) $\omega_y = \pm 0.02$ and (c) $\omega_z = \pm 0.2$, and contours of (d) ω_x, (e) ω_y and (f) ω_z on cylinder surfaces at $Re = 190$ with $L_Z = 4$ (same descriptions as in figure 9).

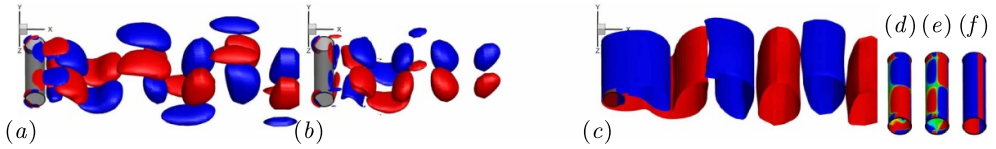

Figure 11. At $t = T_2$, isosurfaces of (a) $\omega_x = \pm 0.02$, (b) $\omega_y = \pm 0.02$ and (c) $\omega_z = \pm 0.2$, and contours of (d) ω_x, (e) ω_y and (f) ω_z on cylinder surfaces at $Re = 190$ with $L_Z = 4$ (same descriptions as in figure 9).

computational errors. Then, for the sake of convenience, the sign of the nonzero vorticity ω is defined by a sign function $\mathrm{sgn}(\omega)$ as:

$$\mathrm{sgn}(\omega) = \begin{cases} 1, & \text{if } \omega > 0, \\ -1, & \text{if } \omega < 0. \end{cases} \tag{4}$$

Finally, in the following content, dominant streamwise and vertical components of vorticity in the shear layers and the near wake mean ω_x and ω_y and their specific signs consistent with those ω_x and ω_y forming pure mode A in the fully developed stage at $Re \geqslant 195$ (Lin and Tan 2019b). While subordinate streamwise and vertical vorticities, mainly distributed behind the rear surface and in the recirculation, just denote ω_x, ω_y, $\mathrm{sgn}(\omega_x)$ and $\mathrm{sgn}(\omega_y)$ inconsistent with those forming pure mode A.

When the wake is fully developed, typical spatiotemporal evolutions of three components of vorticity in the near wake are first presented, typically at $Re = 190$, as shown in figures 9 at T_0, 10 at T_1, 11 at T_2 and 12 at T_3. In particular, at $t = T_1$, through the simple comparison of vorticity isosurfaces and contours on cylinder surfaces with $L_Z = 4$ to those with $L_Z = 12$, as shown in figures 10 and 13, the qualitative distributions of three vorticity signs are totally the same. Moreover, although there is a disturbance vorticity with an intensity about $O(10^{-2})$ near both cylinder ends, typically as shown in figures 13(a) and (b), distributions of three vorticity

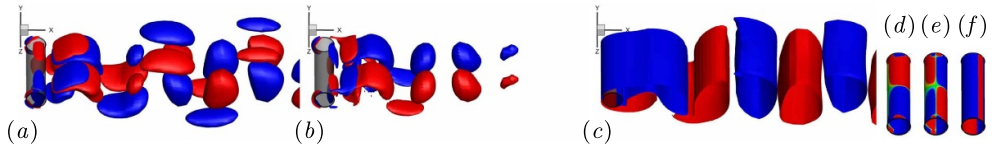

Figure 12. At $t = T_3$, isosurfaces of (a) $\omega_x = \pm 0.02$, (b) $\omega_y = \pm 0.02$ and (c) $\omega_z = \pm 0.2$, and contours of (d) ω_x, (e) ω_y and (f) ω_z on cylinder surfaces at $Re = 190$ with $L_Z = 4$ (same descriptions as in figure 9).

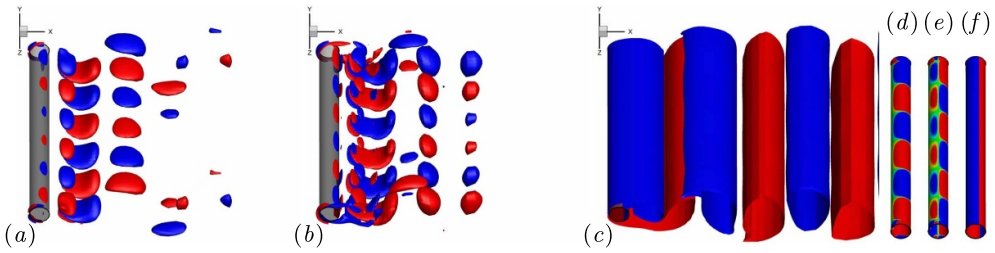

Figure 13. At $t = T_1$, isosurfaces of (a) $\omega_x = \pm 0.02$, (b) $\omega_y = \pm 0.01$ and (c) $\omega_z = \pm 0.2$, and contours of (d) ω_x, (e) ω_y and (f) ω_z on cylinder surfaces at $Re = 190$ with $L_Z = 12$ (same descriptions as in figure 9).

signs in the middle of cylinder are completely unaffected and the same as those near both cylinder ends with $L_Z = 12$, as well as those with $L_Z = 4$ demonstrated in figure 10. Therefore, it clearly indicates that the 3D computations with $L_Z = 4$ are independent of the periodical boundary condition and the spanwise computational length $L_Z = 12$ when Re is less than 195 without the interference of vortex dislocations.

Through comparison with the fully developed stage (Lin and Tan 2019b), the basic and common characteristics of vorticity and its sign relationship in the present stage are summarized as follows:

(a) Symmetry of dominant ω_x and ω_y in the near wake: at the same spanwise position, the sign of dominant ω_x in the upper shear layer and clockwise spanwise vortex (denoted by $y > 0$) is always opposite to that in the lower shear layer and counterclockwise spanwise vortex (denoted by $y < 0$). However, the signs of dominant ω_y in both upper and lower shear layers and both clockwise and counterclockwise spanwise vortices are the same. It should be emphasized here that these additional vorticities, ω_x and ω_y, in a shedding spanwise vortex are also stretched or twisted upstream and convected into an oppositely signed spanwise vortex before shedding, similar to the formation of vortex braids. Therefore, the analysis of the vorticity sign in spatial positions is theoretically ideal, regardless of the above stretching effect of $(\boldsymbol{\omega} \cdot \nabla)\boldsymbol{u}$ and convective transport of $(\boldsymbol{u} \cdot \nabla)\boldsymbol{\omega}$ upstream in equation (3), similar to previous works (Barkley and Henderson 1996, Robichaux *et al* 1999). In other words, in the following analysis, the sign of ω_x or ω_y in the upper or lower shear layer would always be the same as that in the clockwise or counterclockwise spanwise vortex, respectively.

(b) Sign relationship between dominant ω_x and ω_y: in the near wake, $\mathrm{sgn}(\omega_x)$ is the same as $\mathrm{sgn}(\omega_y)$ at $y > 0$ but opposite to $\mathrm{sgn}(\omega_y)$ at $y < 0$, while on the front surface, we have $\mathrm{sgn}(\omega_x) = +\mathrm{sgn}(\omega_y)$ on the upper side and $\mathrm{sgn}(\omega_x) = -\mathrm{sgn}(\omega_y)$ on the lower side.

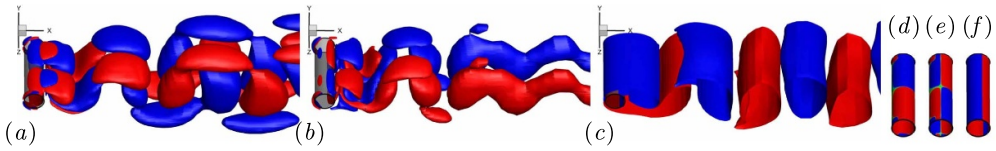

Figure 14. At $t = T_1$, isosurfaces of (a) $\omega_x = \pm 0.02$, (b) $\omega_y = \pm 0.02$ and (c) $\omega_z = \pm 0.2$, and contours of (d) ω_x, (e) ω_y and (f) ω_z on cylinder surfaces at $Re = 192$ with $L_Z = 4$ (same descriptions as in figure 9).

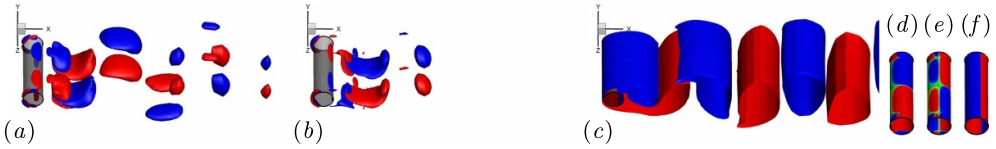

Figure 15. At $t = T_1$, isosurfaces of (a) $\omega_x = \pm 0.02$, (b) $\omega_y = \pm 0.02$ and (c) $\omega_z = \pm 0.2$, and contours of (d) ω_x, (e) ω_y and (f) ω_z on cylinder surfaces at $Re = 185$ with $L_Z = 4$ (same descriptions as in figure 9).

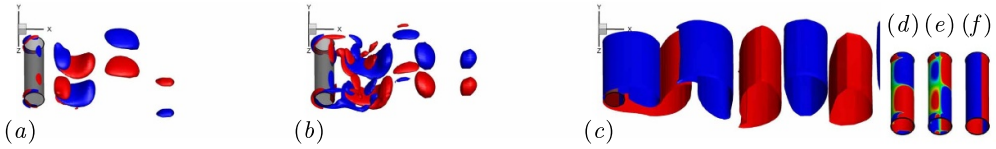

Figure 16. At $t = T_1$, isosurfaces of (a) $\omega_x = \pm 0.02$, (b) $\omega_y = \pm 0.01$ and (c) $\omega_z = \pm 0.2$, and contours of (d) ω_x, (e) ω_y and (f) ω_z on cylinder surfaces at $Re = 180$ with $L_Z = 4$ (same descriptions as in figure 9).

In short, such a sign relationship can be expressed by $\mathrm{sgn}(\omega_x \cdot \omega_y) = +1$ at $y > 0$ and $\mathrm{sgn}(\omega_x \cdot \omega_y) = -1$ at $y < 0$.

(c) Sign relationship between additional vorticities on the rear surface and in the near wake: additional vorticities in the upper or lower shear layer have the same or opposite sign of those on the upper or lower side of rear surface only in a half period of vortex shedding, respectively; for example, at $t = T_1$ and T_2, $-|\omega_x|$ in the upper shear layer at $z = L_Z/4$ has the same sign as ω_x on the rear and upper surface, while in the same period, $-|\omega_y|$ in the upper shear layer at $z = L_Z/4$ has the opposite sign to ω_y on the rear and upper surface.

(d) Sign relationship among dominant ω_x and ω_y and ω_z: under the present circumstances, $-|\omega_z|$ or $+|\omega_z|$ is mainly distributed on the upper or lower and front surface and in the shedding clockwise or counterclockwise spanwise vortex, respectively; therefore, another basic sign relationship, $\mathrm{sgn}(\omega_x \cdot \omega_y \cdot \omega_z) = -1$, is summarized regardless of the vertical position in the near wake, except for the rear surface and recirculation region.

Moreover, at other Reynolds numbers, these features still exist, typically as shown in figures 14 at $Re = 192$, 15 at $Re = 185$ and 16 at $Re = 180$. Until the Reynolds number is less than $160 \sim 170$, additional vorticities are so weak that they totally disappear in the shedding Kármán vortices, as shown in figures 17 and 18. They mainly exist in the shear layers and on

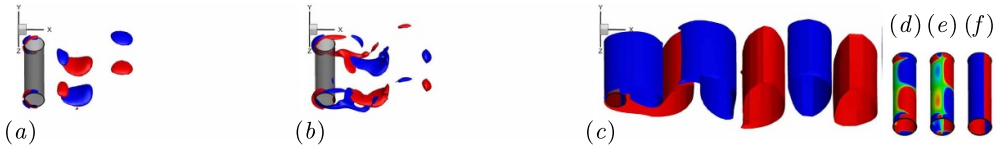

Figure 17. At $t = T_1$, isosurfaces of (a) $\omega_x = \pm 0.02$, (b) $\omega_y = \pm 0.01$ and (c) $\omega_z = \pm 0.2$, and contours of (d) ω_x, (e) ω_y and (f) ω_z on cylinder surfaces at $Re = 170$ with $L_Z = 4$ (same descriptions as in figure 9).

Figure 18. At $t = T_1$, isosurfaces of (a) $\omega_x = \pm 0.02$, (b) $\omega_y = \pm 0.01$ and (c) $\omega_z = \pm 0.2$, and contours of (d) ω_x, (e) ω_y and (f) ω_z on cylinder surfaces at $Re = 160$ with $L_Z = 4$ (same descriptions as in figure 9).

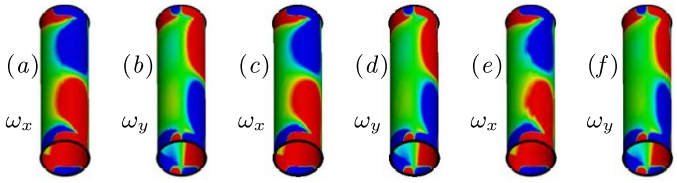

Figure 19. On cylinder surfaces with $L_Z = 4$ at $t = T_1$, contours of (a) ω_x and (b) ω_y at $Re = 155$, contours of (c) ω_x and (d) ω_y at $Re = 150$, and contours of (e) ω_x and (f) ω_y at $Re = 145$, where red and blue colors denote positive and negative values, respectively, and green color denotes $|\omega| < 0.001$. The flow is from left to right.

cylinder surfaces. When the Reynolds number is as low as 150, as shown in figure 19, additional vorticities still exist on cylinder surfaces, indicating that three-dimensional instability already appears at Reynolds numbers lower than 150, also indicated in previous works (Yokoi and Kamemoto 1992, 1993). Nevertheless, two basic sign relationships for dominant ω_x, ω_y and ω_z are still satisfied in the shear layers at $Re \geqslant 160$. Meanwhile, it is interestingly worth noting that the characteristics of these additional vorticities with specific sign distribution on the rear surface are always consistent in the Reynolds number range from 145 to 192. In summary, many similar features clearly illustrate that pure mode A is actually generated at early times or lower Reynolds numbers, and the vorticity on the rear surface of the cylinder related to pure mode A is already generated after three-dimensional instability appears.

However, there are few features different from those in the full development of pure mode A at $Re \geqslant 195$ (Lin and Tan 2019b), summarized as follows:

(a) Shedding spanwise vortices: primary vortex cores are almost undisturbed at present Reynolds numbers (160–192), but a small distortion mainly exists in vortex braids at a certain Reynolds number of approximately 190–192, as shown in figures 10(c), 13(c) and 14(c). This phenomenon clearly shows that the vortex braids first become unstable before primary vortex cores become unstable. The physical reason for undistorted vortex cores is

mainly attributed to the greatly weakened additional vorticities with a magnitude of order of approximately $O(10^{-2})$, even less when the Reynolds number further decreases. Small wavy vortex braids result from the vertical interaction (Lin *et al* 2018) and its superimposition effect due to the same signs of vertical vorticity in both upper and lower shear layers at the same spanwise position.

(b) Surface vorticity: although symmetries of dominant ω_x and ω_y with the wavelength of 4 on cylinder surfaces at $Re = 190$ are almost identical to those in the fully developed stage, as shown in figure 9, disturbed additional vorticities with a small wavelength in both stages appear just out of phase; for example, on the upper surface, disturbed ω_x and ω_y exist at $t = T_0$ in the initial generation stage but at $t = T_2$ in the full development stage. On the other hand, additional vorticities on a certain side of the surface, such as the upper or lower surface, mainly exist for approximately three quarters of the vortex-shedding period.

In summary, the following characteristics or definitions of pure mode A (in the absence of large-scale vortex dislocation interference) can be given for the initial generation stage and the fully developed stage:

(a) The fully developed stage of pure mode A at $Re \geqslant 195$: as reported in previous work (Lin and Tan 2019b), in the near wake at the same spanwise position, there are (a) additional vorticities with the magnitude of $O(10^{-1})$ at the spanwise wavelength λ_A and with the specific sign distributions, such as $\mathrm{sgn}(\omega_x)(y > 0) = -\mathrm{sgn}(\omega_x)(y < 0)$, and $\mathrm{sgn}(\omega_y)(y > 0) = +\mathrm{sgn}(\omega_y)(y < 0)$, (b) the specific sign relationships between ω_x and ω_y, such as $\mathrm{sgn}(\omega_x \cdot \omega_y)(y > 0) = +1$ and $\mathrm{sgn}(\omega_x \cdot \omega_y)(y < 0) = -1$, (c) the wavy primary vortex cores and braids with the special instability wavelength λ_A, and (d) the sudden drop of hydrodynamic parameters (St, $\overline{C}_D$ and C'_L); while on the rear surface at the same spanwise position and $t = T_1$ as an example, there are (e) $\mathrm{sgn}(\omega_x)(y > 0)$ same as that in the upper shear layer but $\mathrm{sgn}(\omega_x)(y < 0)$ opposite to that in the lower shear layer, (f) $\mathrm{sgn}(\omega_y)(y > 0)$ opposite to that in the upper shear layer but $\mathrm{sgn}(\omega_y)(y < 0)$ same as that in the lower shear layer, and therefore (g) $\mathrm{sgn}(\omega_x)(y > 0) = +\mathrm{sgn}(\omega_x)(y < 0)$ and $\mathrm{sgn}(\omega_y)(y > 0) = -\mathrm{sgn}(\omega_y)(y < 0)$;

(b) The initially generated stage of pure mode A at $Re < 195$: as presented above, in the near wake at the same spanwise position when $Re \geqslant 160$, there are (a) additional vorticities with the obviously smaller magnitude of $O(10^{-2})$ at the same spanwise wavelength λ_A and also with the same sign distributions, such as $\mathrm{sgn}(\omega_x)(y > 0) = -\mathrm{sgn}(\omega_x)(y < 0)$, and $\mathrm{sgn}(\omega_y)(y > 0) = +\mathrm{sgn}(\omega_y)(y < 0)$, (b) the totally same sign relationships between ω_x and ω_y, such as $\mathrm{sgn}(\omega_x \cdot \omega_y)(y > 0) = +1$ and $\mathrm{sgn}(\omega_x \cdot \omega_y)(y < 0) = -1$, (c) only the wavy primary vortex braids but with the same instability wavelength λ_A around $Re \sim 190$, and (d) the hydrodynamic parameters completely equivalent to those in 2D flows; while on the rear surface at the same spanwise position and $t = T_1$ as an example, there are also same sign relationships, such as, when $Re \geqslant 160$, (e) $\mathrm{sgn}(\omega_x)(y > 0)$ same as that in the upper shear layer but $\mathrm{sgn}(\omega_x)(y < 0)$ opposite to that in the lower shear layer, and (f) $\mathrm{sgn}(\omega_y)(y > 0)$ opposite to that in the upper shear layer but $\mathrm{sgn}(\omega_y)(y < 0)$ same as that in the lower shear layer, and when $Re \geqslant 145$, (g) $\mathrm{sgn}(\omega_x)(y > 0) = +\mathrm{sgn}(\omega_x)(y < 0)$ and $\mathrm{sgn}(\omega_y)(y > 0) = -\mathrm{sgn}(\omega_y)(y < 0)$. These additional vorticities with the sign relationships, exactly consistent with those in the fully developed stage, appear first on and near the rear surface of the cylinder, then in the shear layers and finally in the shedding spanwise vortices as the Reynolds number increases.

3.3. Critical Reynolds number

The problem of the critical Reynolds number can be analyzed and discussed as follows. The spatiotemporal evolution of additional vorticities in the near wake, as analyzed above, clearly indicates that the critical Reynolds number with the appearance of mode A or 3D wake transition is never a value but an interval or a range, during which pure mode A is initially generated and the wake already becomes three dimensional.

In this stage, the process can be described as follows:

(a) At first, as shown in figure 19, additional vorticities are initially generated on and near cylinder surfaces at a certain lower Reynolds number; in the meantime, dominant ω_x and ω_y almost disappear in the shear layers and shedding spanwise vortices. Therefore, it is intrinsically the moment that three-dimensional instability first appears.
(b) Subsequently, as the Reynolds number increases, as shown in figures 18, 17 and 16, above additional vorticities near cylinder surfaces increase and are convectively transported to the shear layers until they are completely shed, thus entering the shedding primary vortices.
(c) Finally, when the Reynolds number further increases, the intensity of additional vorticities in the shear layers and shedding primary vortices reaches a certain large magnitude, causing the shedding spanwise vortex braids and then cores to be undulating along the span. Therefore, this last process or end moment means that the pure mode A in the initial generation stage has totally evolved into the fully developed pure mode A.

Consequently, this whole process indicates that the spatiotemporal evolution of pure mode A in the initial generation stage is a gradual evolutionary development process starting from three-dimensional instability, instead of suddenly appearing in the near wake.

The Strouhal number, if obtained from the oscillating lift coefficient, cannot capture such a phenomenon in a gradually evolving process, i.e. the initial generation of pure mode A, at $Re < 195$. In fact, the lift coefficient is mainly determined by alternately shedding spanwise vortices without any obvious disturbance of weak additional vorticities. Accordingly, it is necessary to prescribe a different variable suitable for hunting the initially generated stage of pure mode A at lower Reynolds numbers.

With the aid of the RMS lift coefficient over time, some definitions of vorticity intensities in the present flow domain are proposed on the basis of volume integrals. The volume-averaged streamwise and vertical vorticities, $\overline{\omega}_x$ and $\overline{\omega}_y$, respectively, are first defined as:

$$\overline{\omega}_x(t) = \frac{1}{V}\int_V \omega_x \mathrm{d}\tau \approx 0, \tag{5a}$$

$$\overline{\omega}_y(t) = \frac{1}{V}\int_V \omega_y \mathrm{d}\tau \approx 0, \tag{5b}$$

where V is the volume of the flow field of interest, i.e. the whole 3D computational domain, and $\mathrm{d}\tau$ is the volume element. Generally, due to the spanwise periodical flow, $\overline{\omega}_x$ and $\overline{\omega}_y$ are almost (or theoretically) zero or can even be regarded as a kind of computational error from an ideal flow in which $\overline{\omega}_x = \overline{\omega}_y = 0$. For example, at $Re = 190$, $\overline{\omega}_x(T_0) = -5.8 \times 10^{-11}$ and $\overline{\omega}_y(T_0) = -1.2 \times 10^{-8}$, while $\overline{\omega}_x(T_1) = -1.7 \times 10^{-11}$ and $\overline{\omega}_y(T_1) = -6.6 \times 10^{-9}$. Therefore, for the sake of computational convenience, it is assumed in the following results that $\overline{\omega}_x$ and $\overline{\omega}_y$ are zero at any time. The volume-RMS streamwise vorticity, ω_x', the volume-RMS vertical vorticity, ω_y', and the volume-RMS additional vorticity, ω_{xy}', are then defined as:

$$\omega_x'(t) = \sqrt{\frac{1}{V}\int_V (\omega_x - \overline{\omega}_x)^2 \mathrm{d}\tau} \approx \sqrt{\frac{1}{V}\int_V \omega_x^2 \mathrm{d}\tau}, \tag{6a}$$

$$\omega_y'(t) = \sqrt{\frac{1}{V}\int_V (\omega_y - \overline{\omega}_y)^2 \mathrm{d}\tau} \approx \sqrt{\frac{1}{V}\int_V \omega_y^2 \mathrm{d}\tau}, \tag{6b}$$

$$\omega_{xy}'(t) = \sqrt{\frac{1}{V}\int_V [(\omega_x - \overline{\omega}_x)^2 + (\omega_y - \overline{\omega}_y)^2]\,\mathrm{d}\tau} = \sqrt{\omega'^2_x + \omega'^2_y}. \tag{6c}$$

Relations of the above volume-RMS vorticities and their gradients along with the Reynolds number are presented, as shown in figure 20, at two typical times: T_0 (or T_2) and T_1 (or T_3). In the present range of Reynolds numbers from 100 to 210, the variation in the volume-RMS vorticity ω' with the Reynolds number is qualitatively independent of both the vorticity component and time moments. For such variation itself, three different subregions are identified based on the intensity of ω' and its gradient $\mathrm{d}\omega'/\mathrm{d}Re$:

(a) In the first subregion, the Reynolds number is less than 145; the intensity of ω' reaches the magnitude of order $O(10^{-5})$; and as the Reynolds number increases, ω' increases first slowly and then quickly with a gradient of approximately $O(10^{-7}$–$10^{-5})$; meanwhile, the wake pattern is 2D Kármán vortex streets alternately shedding.
(b) The third subregion corresponds to a Reynolds number greater than 195; the strength of ω' is approximately $O(10^{-2})$; similarly, ω' still increases slowly with increasing Reynolds number; and the gradient is approximately $O(10^{-4})$; in the meantime, the wake pattern just corresponds with pure mode A in the fully developed stage.
(c) Between them, there is the second subregion in a range of Reynolds numbers from 145 to 195; as the Reynolds number increases, ω' first slowly increases and then accelerates very quickly as the intensity increases from $O(10^{-4})$ to $O(10^{-2})$; and the largest gradient reaches $O(10^{-2})$ near $Re = 192$–195; at the same time, the wake pattern is in a mixed state, i.e. the initially generated pure mode A, in which the shedding primary vortex cores are still two dimensional while additional vorticities are initially generated due to the activated three-dimensional instability and gradually evolved in the near wake.

According to the above analysis, two critical Reynolds numbers are identified. The first critical Reynolds number Re_{cr0} is (no more than) 145, which indicates the first appearance of the three-dimensional instability on and near cylinder surfaces. The second critical Reynolds number Re_{cr1} is 195 (or less), corresponding to the transition of pure mode A from the initial generation stage to the fully developed stage in the near wake.

In addition, it is necessary to discuss the possible effect of hysteresis on the initially generated pure mode A here. On the one hand, the Reynolds number ranges of the initial appearance of weak additional vorticities in the shear layers and on the rear surface of the cylinder, i.e. $Re \geqslant 160$–170 and $Re \geqslant 145$ in figures 17, 18 and 19, respectively, actually exceeds the Reynolds number range of hysteresis in experiment (Williamson 1996a), i.e. $Re = 180$–190. This indicates the initial appearance of additional vorticities at lower Reynolds numbers physically irrelevant to the hysteresis. On the other hand, the determination of Re_{cr} in the hysteresis is closely dependent on the initial condition. As stated in previous work (Williamson 1996a), the exact Re_{cr} depends on whether the flow speed is increased or decreased. In present work, the inflow speed is constant as the inlet boundary condition, same as that in previous work (Jiang *et al* 2016). The influence of variable incoming velocity or Reynolds number, as the initial condition, on the determination of Re_{cr} and the appearance of additional vorticities in

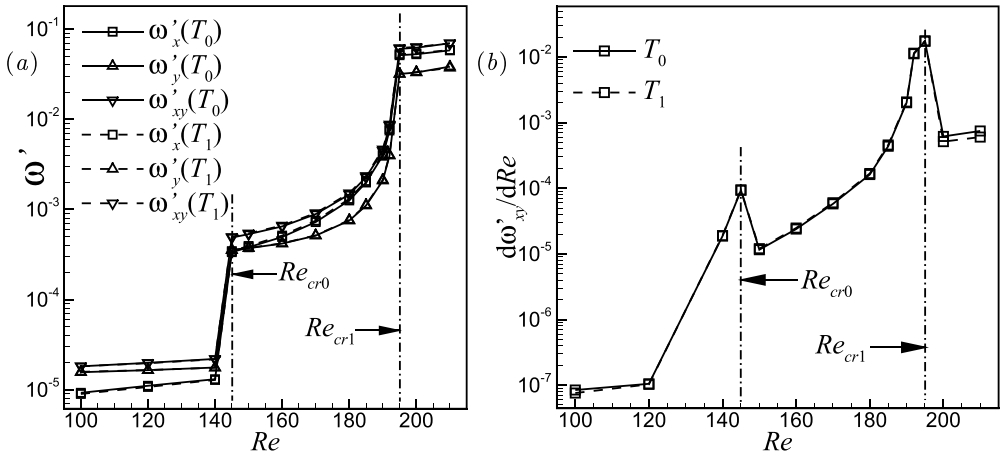

Figure 20. (a) Volume-RMS vorticities in equation (6) and (b) the gradient of the xy component (ω'_{xy}) along with Re at two typical times, $t = T_0$ (or T_2) and T_1 (or T_3), with $L_Z = 4$.

the shear layers and on the rear surface of the cylinder would be investigated in the future work.

3.4. Formation and shedding sequences of vorticity

First of all, some labels in figures are described as follows:

- VorXs-U and VorXs-D: subordinate ('s') ω_x ('VorX') on the upper ('U') and down ('D') or lower sides of the wake center plane $y = 0$, respectively;
- VorX0-U and VorX0-D: dominant ω_x initially generated and/or increasing in the upper ('U') and lower ('D') shear layers, respectively;
- VorX1-U and VorX1-D: dominant ω_x concentrated and/or immediately shedding from the upper ('U') and lower ('D') shear layers, respectively.

Similar meanings of labels, VorY0-U, VorY1-U, VorYs-U, VorY0-D, VorY1-D and VorYs-D, are prescribed for the vertical vorticity ('VorY') behind the cylinder.

Typically at $Re = 190$, additional vorticities near the cylinder and in the shear layers are investigated at $z = L_Z/4$ $(= 1)$ during a whole vortex-shedding period, as shown in figures 21–26, with typical times illustrated in figure 4. Physical formations of dominant ω_x and ω_y in the shear layers can be demonstrated in the temporal evolution.

For dominant ω_x, as a typical example, in the lower shear layer, the formation process is elaborated first:

(a) At $t = T_1$, as shown in figure 23(a), $+|\omega_x|$ in 'VorX0-D' with weak intensity is just initially generated in the lower shear layer. The obvious feature is the opposite sign relationship between 'VorX0-D' and $-|\omega_x|$ on the rear and lower surfaces. It should be noticed that the location of the initially appearing 'VorX0-D' is approximately $(x = 0.6, y = -0.6)$, while the location of the anticlockwise spanwise vortex core which is already formed in the lower shear layer is near $(x = 3, y = 0)$ downstream. This feature obviously disagrees with previous viewpoints (Williamson 1996a, Leweke and Williamson 1998).

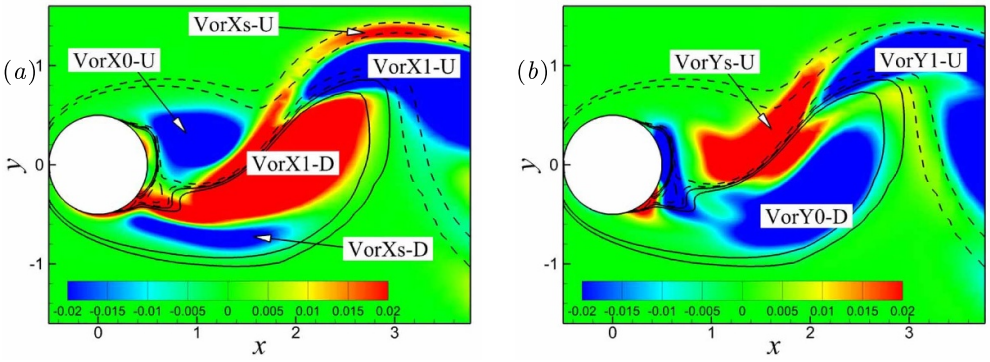

Figure 21. Color contours of (a) ω_x and (b) ω_y at $z = 1$, $t = T_0$ and $Re = 190$ with $L_Z = 4$, where solid and dashed contours of $\omega_z = \pm 0.1$ and ± 0.5 denote positive and negative values, respectively.

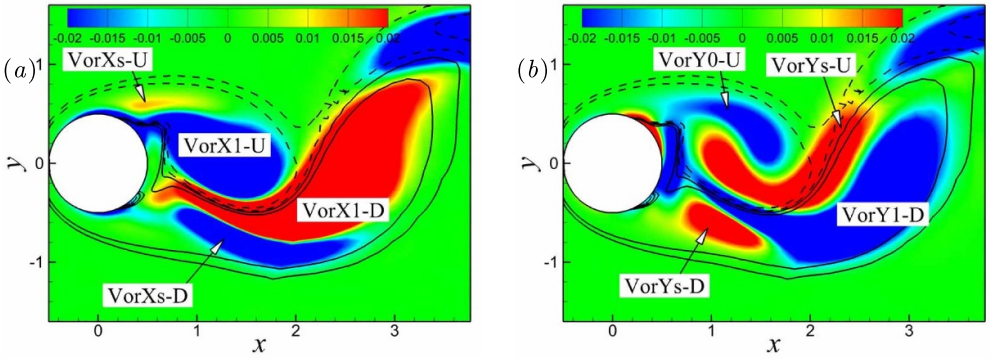

Figure 22. Color contours of (a) ω_x and (b) ω_y at $z = 1$, $t \in (T_0, T_1)$ and $Re = 190$ with $L_Z = 4$ (same description as in figure 21).

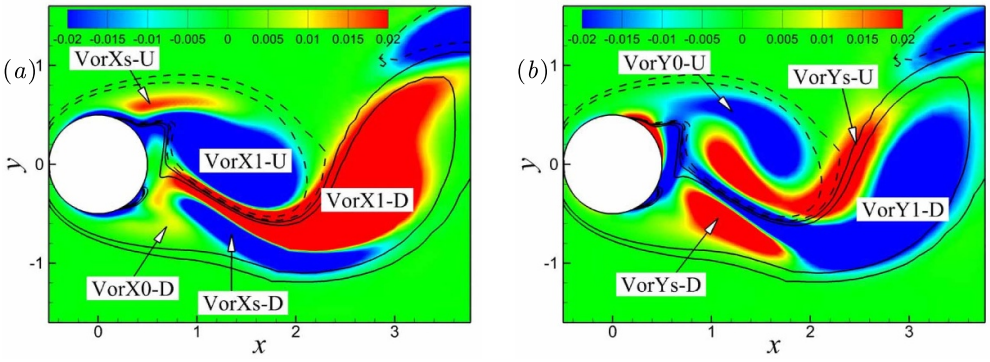

Figure 23. Color contours of (a) ω_x and (b) ω_y at $z = 1$, $t = T_1$ and $Re = 190$ with $L_Z = 4$ (same description as in figure 21).

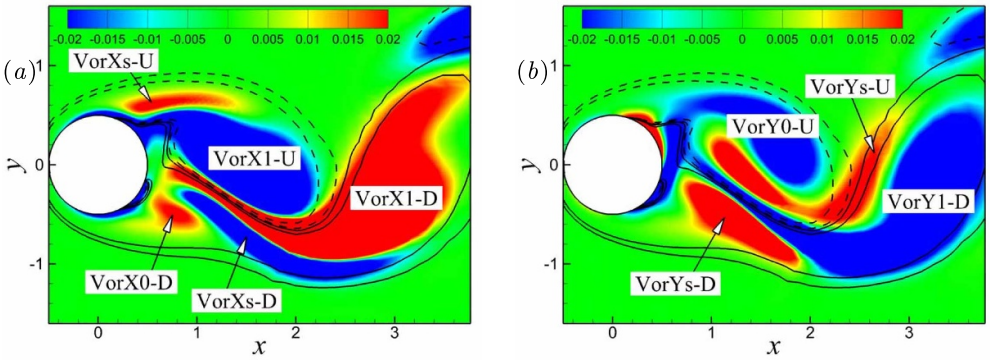

Figure 24. Color contours of (a) ω_x and (b) ω_y at $z = 1$, $t \in (T_1, T_2)$ and $Re = 190$ with $L_Z = 4$ (same description as in figure 21).

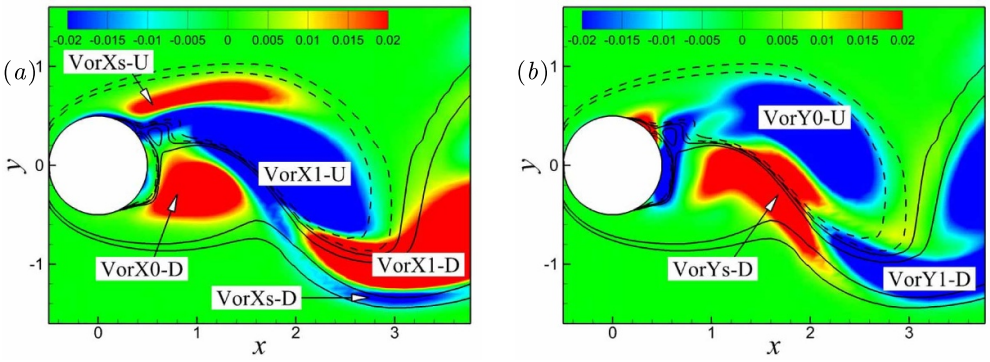

Figure 25. Color contours of (a) ω_x and (b) ω_y at $z = 1$, $t = T_2$ and $Re = 190$ with $L_Z = 4$ (same description as in figure 21).

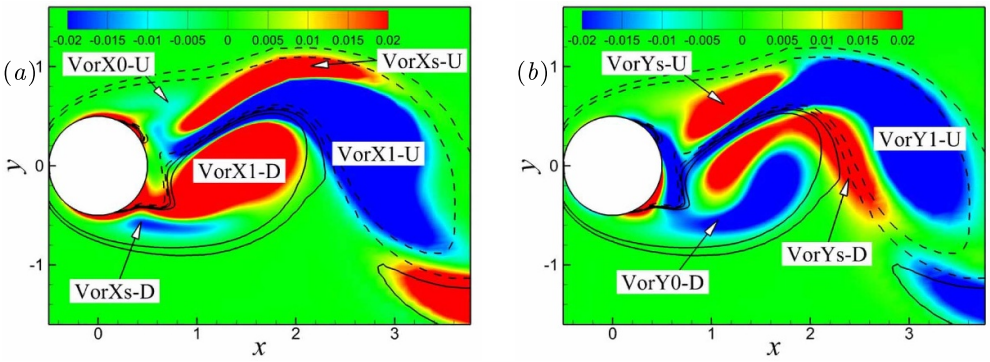

Figure 26. Color contours of (a) ω_x and (b) ω_y at $z = 1$, $t = T_3$ and $Re = 190$ with $L_Z = 4$ (same description as in figure 21).

(b) As time proceeds from T_1 up to T_2, $+|\omega_x|$ in 'VorX0-D' gradually increases, as shown in figures 24(a) and 25(a). Until this point, sgn(ω) in 'VorX0-D' and on the rear and lower surfaces is the opposite.
(c) At time T_3, as shown in figure 26(a), the original 'VorX0-D' becomes 'VorX1-D'. The obvious different feature is that sgn(ω_x) in 'VorX1-D' and on the rear and lower surfaces is exactly the same.
(d) At $t = T_4$ or T_0, as shown in figure 21(a), 'VorX1-D' is about to shed from the cylinder, as well as increasing the counterclockwise spanwise vortex.
(e) When the time exceeds T_0 but is less than T_1, as shown in figure 22(a), 'VorX1-D', increasing due to the stretching effect of $(\boldsymbol{\omega}\cdot\nabla)\boldsymbol{u}$ in equation (3), and the counterclockwise Kármán vortex completely sheds from the cylinder.

Then, the formation process of dominant ω_y in the upper shear layer, as an instance, can be elaborated:

(a) At a certain time in a range from T_0 to T_1, 'VorY0-U' is initially generated in the upper shear layer, as shown in figure 22(b). Its sign is completely the same as that of ω_y on the rear and lower surfaces.
(b) With the passage of time from T_1 to T_2, 'VorY0-U' gradually increases, as shown in figures 23(b), 24(b) and 25(b). During this period, sgn(ω_y) in 'VorY0-U' and on the rear and lower surfaces is always the same.
(c) At $t = T_3$ and subsequent T_4 (or T_0), as shown in figures 26(b) and 21(b), 'VorY0-U' has already become 'VorY1-U' and sheds with a clockwise spanwise vortex.

Based on the above analysis, the formation and shedding sequences of the dominant ω_x and ω_y in the shear layers can be summarized in table 2 over the whole vortex-shedding period in figure 4. In particular, asynchronization in the initial generation of dominant ω_x and ω_y in a certain shear layer is observed and should be taken into account, such as in the upper shear layer shown in figures 22 and 26. The results clearly indicate that in the present initially generated pure mode A, such as at $Re = 190$, dominant ω_x and ω_y on the same side of shear layers are initially generated with time difference $T_{\mathrm{XE}} - T_{\mathrm{YS}}$ (upper side) or $T_{\mathrm{XS}} - T_{\mathrm{YE}}$ (lower side), but shedding with phase difference $T_{\mathrm{XE}} - T_{\mathrm{YE}}$ (upper side) or $T_{\mathrm{XS}} - T_{\mathrm{YS}}$ (lower side) or less. These values are different from those in the fully developed pure mode A (Lin and Tan 2019b).

3.5. *Origins of dominant ω_x and ω_y in the shear layers*

According to the above formation process of dominant ω_x and ω_y in the shear layers, the physical origin of dominant ω_x, as an example of 'VorX0-D' in the lower shear layer from T_1 to T_2, as shown in figures 23(a), 24(a) and 25(a), is first analyzed and discussed as follows:

(a) Because opposite sign relationships exist between ω_x in 'VorX0-D' and on the rear and lower surfaces, the mechanism of vorticity generation at walls is invalid.
(b) As shown in figure 27, the local velocity vector clearly indicates that 'VorX0-D' gradually increases relatively upstream of 'VorX1-D'. This indicates that vorticity in 'VorX0-D' upstream cannot originate or be convected from that in 'VorX1-D' downstream. Otherwise, 'VorX0-D' should already be generated early at $t < T_1$. In fact, this generation mechanism never occurs, as shown in figure 22(a).

Table 2. Summary of the formation and shedding process of streamwise and vertical vorticities in the upper ($y>0$) and lower ($y<0$) shear layers in a whole cycle of the initially generated pure mode A (typically at $Re=190$), associated with alternately shedding spanwise vortices with vorticity $\pm|\omega_z|$, where labels, 'Ap', 'In', and 'Sh' in brackets, denote the vorticity initially appearing, increasing and shedding, respectively, and symbol $\mapsto$ indicates the transformed or evolved process.

t	T_{YS}	$T_{\mathrm{YS}}\rightarrow T_{\mathrm{XS}}$
$y>0$	VorX0-U(In), VorX1-U(Sh)	VorX0-U(In), VorX1-U(Sh)
	VorY0-U(Ap)	VorY0-U(In)
	$-\|\omega_z\|$(In)	$-\|\omega_z\|$(In)
$y<0$	VorX1-D(In/Sh)	VorX1-D(In/Sh)
	VorY0-D $\mapsto$ VorY1-D	VorY1-D(Sh)
	$+\|\omega_z\|$(Sh)	$+\|\omega_z\|$(Sh)
t	T_{XS}	$T_{\mathrm{XS}}\rightarrow T_1\rightarrow T_2\rightarrow T_{\mathrm{YE}}$
$y>0$	VorX0-U $\mapsto$ VorX1-U	VorX1-U(In)
	VorY0-U(In)	VorY0-U(In)
	$-\|\omega_z\|$(In)	$-\|\omega_z\|$(In)
$y<0$	VorX0-D(Ap), VorX1-D(Sh)	VorX0-D(In), VorX1-D(Sh)
	VorY1-D(Sh)	VorY1-D(Sh)
	$+\|\omega_z\|$(Sh)	$+\|\omega_z\|$(Sh)
t	T_{YE}	$T_{\mathrm{YE}}\rightarrow T_{\mathrm{XE}}$
$y>0$	VorX1-U(In/Sh)	VorX1-U(In/Sh)
	VorY0-U $\mapsto$ VorY1-U	VorY1-U(Sh)
	$-\|\omega_z\|$(Sh)	$-\|\omega_z\|$(Sh)
$y<0$	VorX0-D(In), VorX1-D(Sh)	VorX0-D(In), VorX1-D(Sh)
	VorY0-D(Ap)	VorY0-D(In)
	$+\|\omega_z\|$(In)	$+\|\omega_z\|$(In)
t	T_{XE}	$T_{\mathrm{XE}}\rightarrow T_3\rightarrow T_4\rightarrow T_{\mathrm{YS}}$
$y>0$	VorX0-U(Ap), VorX1-U(Sh)	VorX0-U(In), VorX1-U(Sh)
	VorY1-U(Sh)	VorY1-U(Sh)
	$-\|\omega_z\|$(Sh)	$-\|\omega_z\|$(Sh)
$y<0$	VorX0-D $\mapsto$ VorX1-D	VorX1-D(In)
	VorY0-D(In)	VorY0-D(In)
	$+\|\omega_z\|$(In)	$+\|\omega_z\|$(In)

(c) Moreover, as shown in figures 14, 10, 15, 16, 17 and 18 with decreasing Reynolds number, additional vorticities in the shedding spanwise vortices are gradually weakened and even only exist in the shear layers at $Re=160$. This suggests that streamwise vorticity in shedding spanwise vortices is convectively transported from that in the shear layers, rather than Biot–Savart induction from streamwise vorticity in the downstream spanwise vortex to that in the upstream spanwise vortex successively under a self-sustained effect (Williamson 1996a, Leweke and Williamson 1998, Thompson *et al* 2001, Jiang *et al* 2016, 2018).

(d) Based on the theory of the vortex-induced vortex (VIVor) (Lin *et al* 2019a, 2019c), as time proceeds from T_0 to T_2, as shown in figures 22(a), 27(a) and 27(b), there are two

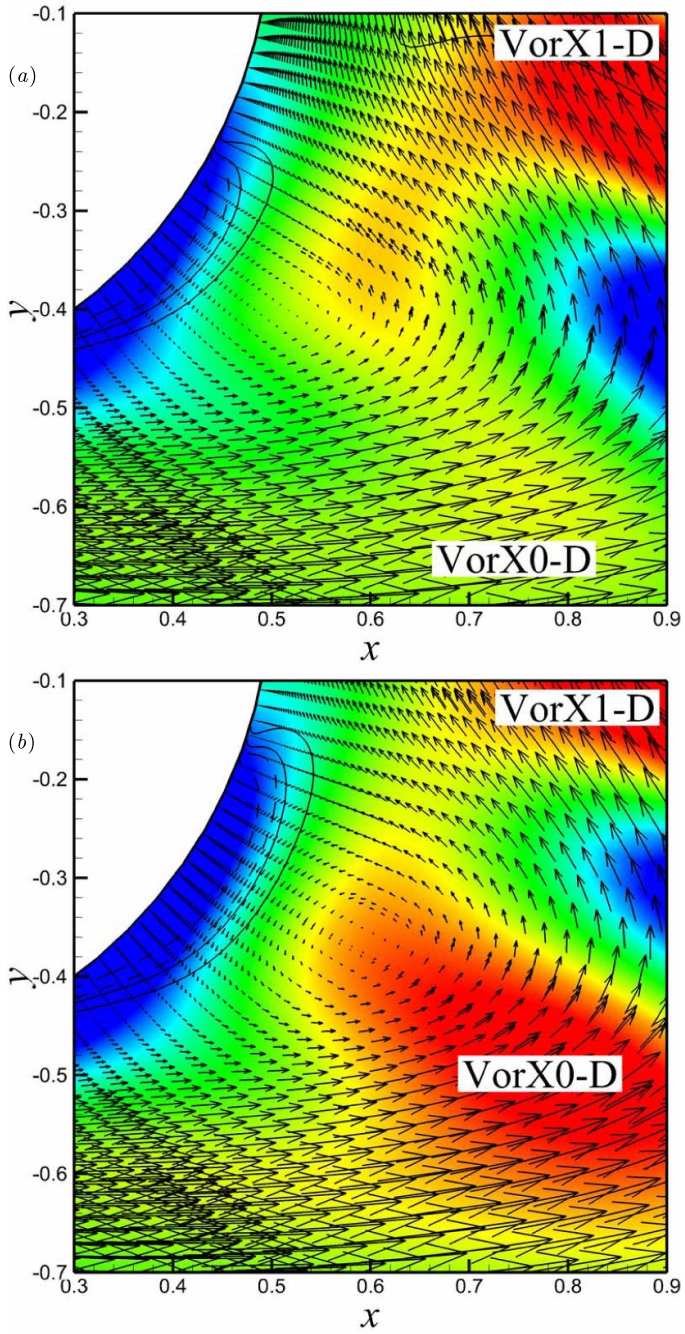

Figure 27. At $z = 1$ and $Re = 190$ with $L_Z = 4$, color contours of ω_x and local velocity vector denoted by arrows at (a) $t = T_1$ and (b) $t \in (T_1, T_2)$ (same descriptions as in figure 21) with same legends in figures 23(a) and 24(a), respectively.

key factors. The first factor is the gradually increasing $-|\omega_y|$ on the rear and lower surfaces from $y = -0.3$ in figure 22(b) to $y = -0.5$ in figure 23(b). The second factor is the increasing convective transport according to the local velocity vector in figure 27 near the rear and lower surface and then in the lower shear layer. These two factors result in $+|\omega_x|$ in 'VorX0-D' being initially induced by $-|\omega_y|$ on the rear and lower surfaces and then evolving under the local inertial convective effect. On the other hand, the vertical position of maximal vorticity in 'VorX0-D' also qualitatively agrees with the prediction of the VIVor mechanism, i.e. the downstream position of vertical vorticity and away from the surface.

(e) However, as time passes following T_3 and T_0, as shown in figures 26(a) and 21(a), $+|\omega_x|$ in 'VorX1-D' is apparently convected from the region enclosing the rear and lower surfaces, which is consistent with experimental observations about vorticity generated at walls (Yokoi and Kamemoto 1992, 1993).

Thus, dominant streamwise vorticity in the shear layers is first induced by dominant vertical vorticity on the rear surface under the VIVor mechanism coupled with the inertial convective effect over a half period and then further increases through the nonlinear convective transport of streamwise vorticity on the rear surface over the rest of the half period. This process in the present initially generated stage is consistent with that in the fully developed stage (Lin and Tan 2019b).

In summary, three evidences obtained in present study disagree with the point of view reported in previous works (Williamson 1996a, Leweke and Williamson 1998, Thompson *et al* 2001, Jiang *et al* 2016, 2018). The first evidence is the appearance of additional vorticities, consistent with those in the fully developed pure mode A, in the near wake before the primary vortex cores become unstable, reported in section 3.2. The second evidence is the initially generated streamwise vorticity completely upstream of the already formed spanwise vortex core, given in section 3.4. The third evidence is the streamwise vorticity in the shedding spanwise vortex actually originated from that in the shear layer through the convective transportation, provided in present subsection. Therefore, as Reynolds number increases, the physical sequence actually is the initial appearance of streamwise vorticity in the shear layers before primary vortex cores become unstable, then the unstable and wavy vortex braids and finally the unstable primary vortex cores when additional vorticities in shedding vortices reach a certain magnitude.

The origin of dominant ω_y in the shear layers is relatively simple. The physical origin is simply the basic vorticity generation at walls and coupled convective transport from vertical vorticity on the opposite side of cylinder surfaces, as shown in figures 22(b) and 26(b). This is also consistent with the case of the fully developed pure mode A (Lin and Tan 2019b).

4. Conclusions

In this paper, the initially generated pure mode A as the transitional stage in the 3D wake transition of a circular cylinder is mainly investigated. Direct numerical simulations with computational spanwise lengths of four diameters are mainly performed in a range of Reynolds numbers from 100 to 210.

Through the analysis of the force histories and frequency, two wake stages with the occurrence of pure mode A are identified, i.e. the initial generation stage and the full development

stage. In the initially generated stage, the hydrodynamic parameters are almost equivalent to those in 2D wake flow at a Reynolds number less than 195. In the fully developed stage, these hydrodynamic parameters all suddenly drop when $Re \geqslant 195$.

From the viewpoint of the spatiotemporal evolution of vorticity and its sign, most of the features appearing in the present initial generation of pure mode A are consistent with those in the fully developed stage of pure mode A. For example, in the initially generated stage, the spatial symmetry of additional vorticities in the near wake shows that streamwise vortices at opposite signs on both sides of the wake center plane are alternately shed, while vertical vortices with the same signs are parallel to each other. For special sign relationships between streamwise and vertical vorticities, the sign of streamwise vorticity is always the same as that of vertical vorticity in the upper shear layer but opposite to that of vertical vorticity in the lower shear layer. Therefore, the present numerical simulations confirm that pure mode A actually appears in the near wake at a low Reynolds number less than 195, even $160 \sim 170$, as well as three-dimensional instability on cylinder surfaces. In summary, the pure mode A appearing in the near wake is a gradual process, rather than a suddenly changing process accompanied by a sudden drop in the vortex shedding frequency or the instability of primary vortex cores. Moreover, with the increasing Reynolds number, additional vorticities in pure mode A first appear on and near cylinder surfaces, then in the shear layers, and finally in the shedding spanwise vortices, instead of appearing suddenly in the shedding primary vortices after the primary vortex cores become unstable.

To capture such a transitional stage in pure mode A at low Reynolds numbers, volume-RMS vorticities are proposed. As the vorticity varies with the Reynolds number, strengths of additional vorticities in the wake gradually increase first slowly and then quickly when Reynolds number gradually approaches 145, then increasingly gradually in a similar manner in a range of Reynolds numbers from 145 to 195 and finally slowly again at Reynolds number greater than 195. This clearly presents two critical Reynolds numbers in such a progress. The first critical Reynolds number Re_{cr0} is 145 (at most), indicating the initial appearance of three-dimensional instability on and near cylinder surfaces. The second critical Reynolds number Re_{cr1} is 195 (at most), illustrating the transition of pure mode A from the initial generation stage to the full development stage.

In the analysis of the formation and shedding sequences of additional vorticities in the shear layers, there is little difference from those in the fully developed pure mode A because of the asynchronization in the initial generation of dominant streamwise and vertical components of vorticity on opposite sides of shear layers in the present initial generation stage.

Finally, according to formation and shedding sequences, the physical origins of dominant additional vorticities in the present initially generated stage are consistent with those in the fully developed pure mode A. For example, dominant streamwise vorticity in the shear layers is first induced by the vertical vorticity on the rear surface under the vortex-induced vortex mechanism and evolves under the inertial convective effect over one half period and then increases owing to the convective transport of streamwise vorticity on the rear surface over another half period.

ORCID iD

L M Lin https://orcid.org/0000-0001-8933-9630

References

Agbaglah G and Mavriplis C 2017 Computational analysis of physical mechanisms at the onset of three-dimensionality in the wake of a square cylinder *J. Fluid Mech.* **833** 631–47

Agbaglah G and Mavriplis C 2019 Three-dimensional wakes behind cylinders of square and circular cross-section: early and long-time dynamics *J. Fluid Mech.* **870** 419–32

Barkely D and Henderson R D 1996 Three-dimensional Floquet stability analysis of the wake of a circular cylinder *J. Fluid Mech.* **322** 215–41

Barkley D, Tuckerman L S and Golubitsky M 2000 Bifurcation theory for three-dimensional flow in the wake of a circular cylinder *Phys. Rev.* E **61** 5247–52

Clainche S L, Pérez J M and Vega J M 2018 Spatio-temporal flow structures in the three-dimensional wake of a circular cylinder *Fluid Dyn. Res.* **50** 051406

Darekar R M and Sherwin S J 2001 Flow past a square-section cylinder with a wavy stagnation face *J. Fluid Mech.* **426** 263–95

Henderson R D 1997 Nonlinear dynamics and pattern formation in turbulent wake transition *J. Fluid Mech.* **352** 65–112

Jiang H and Cheng L 2019 Transition to the secondary vortex street in the wake of a circular cylinder *J. Fluid Mech.* **867** 691–722

Jiang H, Cheng L, Draper S and An H 2017 Prediction of the secondary wake instability of a circular cylinder with direct numerical simulation *Comput. Fluids* **149** 172–80

Jiang H, Cheng L, Draper S, An H and Tong F 2016 Three-dimensional direct numerical simulation of wake transitions of a circular cylinder *J. Fluid Mech.* **801** 353–91

Jiang H Y, Cheng L and An H W 2018 Three-dimensional wake transition of a square cylinder *J. Fluid Mech.* **842** 102–27

Karniadakis G E and Triantafyllou G S 1992 Three-dimensional dynamics and transition to turbulence in the wake of bluff bodies *J. Fluid Mech.* **238** 1–30

Leweke T and Williamson C H K 1998 Three-dimensional instabilities in wake transition *Eur. J. Mech.* B **17** 571–86

Lin L M, Shi S Y and Wu Y X 2019a Physical mechanism for origin of streamwise vortices in mode A of a square-section cylinder *Acta Mech. Sin.* **35** 411–8

Lin L M, Shi S Y, Zhong X F and Wu Y X 2019c Mechanism of wavy vortex and sign laws in flow past a bluff body: vortex-induced vortex *Acta Mech. Sin.* **35** 1–14

Lin L M and Tan Z R 2019b DNS in evolution of vorticity and sign relationship in wake transition of a circular cylinder: (pure) mode A *Acta Mech. Sin.* **35** 1131–49

Lin L M and Tan Z R 2022 DNS of the spatiotemporal evolution of the vorticity in (pure) mode B of a circular cylinder's wake *Fluid Dyn. Res.* **54** 015511

Lin L M, Zhong X F and Wu Y X 2018 Effect of perforation on flow past a conic cylinder at $Re = 100$: wavy vortex and sign laws *Acta Mech. Sin.* **34** 812–29

Ling G C and Chang Y 1999 Three-dimensional stability analysis of the periodic wake behind a circular cylinder by low-dimensional Galerkin method *Chin. J. Theor. Appl. Mech.* **31** 652–60

Luo S C, Chew Y T and Ng Y T 2003 Characteristics of square cylinder wake transition flows *Phys. Fluids* **15** 2549–59

Meiburg E and Lasheras J C 1988 Experimental and numerical investigation of the three-dimensional transition in plane wakes *J. Fluid Mech.* **190** 1–37

Persillon A and Braza M 1998 Physical analysis of the transition to turbulence in the wake of a circular cylinder by three-dimensional Navier–Stokes simulation *J. Fluid Mech.* **365** 23–88

Posdziech O and Grundmann R 2001 Numerical simulation of the flow around an infinitely long circular cylinder in the transition regime *Theor. Comput. Fluid Dyn.* **15** 121–41

Prasad A and Williamson C H K 1997 Three-dimensional effects in turbulent bluff-body wakes *J. Fluid Mech.* **343** 235–65

Rao A, Thompson M C, Leweke T and Hourigan K 2013 The flow past a circular cylinder translating at different heights above a wall *J. Fluids Struct.* **41** 9–21

Robichaux J, Balachandar S and Vanka S P 1999 Three-dimensional Floquet instability analysis of the wake of square cylinder *Phys. Fluids* **11** 560–78

Sheard G J, Thompson M C and Hourigan K 2003 A coupled Landau model describing the Strouhal–Reynolds number profile of a three-dimensional circular cylinder wake *Phys. Fluids* **15** L68–L71

Thompson M C, Leweke T and Williamson C H K 2001 The physical mechanism of transition in bluff body wakes *J. Fluids Struct.* **15** 607–16
Williamson C H K 1996a Vortex dynamics in the cylinder wake *Annu. Rev. Fluid Mech.* **28** 477–539
Williamson C H K 1996b Three-dimensional wake transition *J. Fluid Mech.* **328** 345–407
Wu Z B and Ling G C 1993 Numerical study on the mechanism for three-dimensional evolution of vortex and the structural features in the wake behind a circular cylinder *Chin. J. Theor. Appl. Mech.* **25** 264–75
Yokoi Y and Kamemoto K 1992 Initial stage of a three-dimensional vortex structure existing in a two-dimensional boundary layer separation flow (observation of laminar boundary layer separation over a circular cylinder by flow visualization) *JSME Int. J.* II **35** 189–95
Yokoi Y and Kamemoto K 1993 Initial stage of a three-dimensional vortex structure existing in a two-dimensional boundary layer separation flow (visual observation of laminar boundary layer separation over a circular cylinder from the side of a separated region) *JSME Int. J.* B **36** 201–6